PAPER

Excitation of external kink mode by trapped energetic particles

To cite this article: S.C. Guo *et al* 2016 *Nucl. Fusion* **56** 056006

View the article online for updates and enhancements.

Excitation of external kink mode by trapped energetic particles

S.C. Guo[1], X.Y. Xu[1], Y.Q. Liu[2] and Z.R. Wang[3]

[1] Consorzio RFX, Corso Stati Unit 4, 35127 Padova, Italy
[2] CCFE, Culham Science Centre, Oxon OX14 3DB, UK
[3] Princeton Plasma Physics Laboratory, Princeton, NJ 08543, USA

E-mail: shichong.guo@igi.cnr.it

CrossMark

Abstract

An unstable fishbone-like non-resonant external kink mode (FLEM) is numerically found to be driven by the precessional drift motion of trapped energetic particles (EPs) in both reversed-field pinch (RFP) and tokamak plasmas, even under the ideal wall boundary condition. In the presence of a sufficiently large fraction of trapped energetic ions in high beta plasmas, the FLEM instability may occur. The excitation condition is discussed in detail. The frequency of the FLEM is linked to the precessional drift frequency of EPs, and varies with the plasma flow speed. Therefore, it is usually much higher than that of the typical resistive wall mode (RWM). In general, the growth rate of FLEM does not depend on the wall resistivity. However, the wall position can significantly affect the mode's property. The drift kinetic effects from thermal particles (mainly due to the transit resonance of passing particles) play a stabilizing role on FLEMs. In the presence of EPs, the FLEM and the RWM can co-exist or even couple to each other, depending on the plasma parameters. The FLEM instabilities in RFP and tokamaks have rather similar physics nature, although certain sub-dominant characters appear differently in the two configurations.

Keywords: 52.30.Cv magnetohydrodynamics, 52.35.Py macroinstabili7es, 52.55.Tn ideal and resistive MHD modes, kinetic modes, 52.65.Ww hybrid methods, 52.25.Dg plasma kinetic equations

(Some figures may appear in colour only in the online journal)

1. Introduction

The energetic particle (EP) physics is one of the key issues in understanding the behavior of burning plasmas, representing the primary scientific challenge faced by ITER and fusion research in general. On the one hand, the self-heating in a fusion reactor is provided by alphas generated at 3.5MeV by the *D–T* fusion reactions; other energetic ions, generated by neutral beam injection (NBI) and ion cyclotron resonant heating (ICRH), are expected to play a major role in achieving optimal burning plasma scenarios with external heating and/or current drive. On the other hand, EPs often interact with bulk plasma waves and instabilities, leading to their destabilization or stabilization, or even to excitation of new types of instabilities. Such an interaction also often results in redistribution and losses of EPs.

It is well known that future advanced tokamak (AT) devices need to operate under steady-state conditions, and at rather high-β ($\beta = 2\mu_0 P/B^2$ is the ratio of the plasma pressure to the magnetic field pressure). However, the achievable maximal β is often limited by macroscopic magnetohydrodynamics (MHD) instabilities such as the external kink mode [1], which causes a global distortion of the plasma that often results in a major disruption. Below a certain threshold value of β—the so-called ideal wall beta limit—the external kink mode is completely stabilized by a perfectly conducting wall located near the plasma surface, according to ideal MHD theory. The mode, however, can convert into other unstable branches under certain circumstances. The most well-known destabilizing mechanism is the replacement of the ideal wall with a realistically existing resistive wall in experimental fusion devices. A resistive wall allows the magnetic perturbation of the kink

instability to penetrate through, leading to a slowly growing instability called the resistive wall mode (RWM) [1, 2].

Another destabilizing mechanism, which we shall study in this work, comes from the precessional drift motion of trapped energetic ions. This mechanism induces instability of a new branch of the external kink mode, even under an ideal wall assumption. This branch, in many aspects, resembles the classical fishbone instability, which was experimentally observed [3] and theoretically well studied around the 1980s [4, 5]. It was understood that trapped EPs provide an additional destabilization mechanism to a fluid-wise stable internal kink mode, producing a new unstable branch called a fishbone. In the following text, we use the name 'Fishbone-like external kink mode (FLEM)' referring to the above-mentioned external kink instability excited by the trapped EPs.

In recent tokamak experiments, a new fishbone-like bursting mode was observed and investigated in NBI heated plasmas [6–9]. Theoretical study [10, 11] also found a new branch in the presence of trapped EPs, based on analytic solutions of the RWM dispersion relation. Furthermore, an unexpected high-frequency (comparable to the geodesic acoustic mode and beta-induced Alfven eigenmode) fishbone has also been observed in JET experiments, with a theoretical interpretation based on a new suitable dispersion relation [12–14]. In reversed-field pinch (RFP) configuration, NBI has only recently been applied on the Madison symmetric torus (MST) experiments, with the observation of EP-induced MHD fluctuations [15–17]. All the above results provided useful insight into the physics of EPs interacting with global MHD modes. Certainly, this is a vast problem that still remains to be further investigated.

In this work, we numerically study, in full toroidal geometry, the excitation of MHD external kink modes by energetic ions, in both RFP and tokamak plasmas. Moreover, we also compare the EP kinetic effects between these two configurations. This study provides a possible explanation on the above fish-bone-like bursting recently observed in tokamak experiments, meanwhile predicting the EP-driven FLEM instability in RFP plasmas. Thus, the results should be well relevant to the present and future experiments in the presence of EPs.

The toroidal stability code MARS-K [18] is adopted for this study. The drift kinetic physics from both energetic ions and bulk thermal particles are self-consistently treated in the MARS-K formulation. The numerical analyses clarify the driven mechanism of FLEM, which is distinguished from that of RWMs. The FLEM satisfies the external kink dispersion relation, in which the kinetic effects of the hot ions are included. The kinetic contribution by trapped hot ions is a unique destabilizing (driving) mechanism for the FLEM instability. While for the RWM, the precession resonance of the trapped hot ions alone can only play a stabilizing (damping) role through their kinetic contribution to the energy balance as represented by the dispersion relation. The varied physics nature of FLEM is further clarified, and its relation (co-existence/coupling) with the RWM is also investigated.

In the following discussion we differentiate the poloidal harmonics of the external kink modes from the 'non-resonant mode' with the 'resonant-mode'. The former have their

rational surfaces (surface of $\mathbf{k} \cdot \mathbf{B} = 0$, $\mathbf{k}$ is mode number, $\mathbf{B}$ is the magnetic field) located outside the plasma, while the latter have their rational surfaces located inside the plasma.

The paper is organized as follows. Section 2 describes the theoretical formulation related to the MHD-kinetic hybrid model, as well as the equilibrium models of EPs used in this work. Section 3 is devoted to the investigation of the FLEM in RFP configuration. The physics mechanism of the FLEM triggering, as well as the nature of the instability, is discussed. The possibility of co-existence/coupling with RWM is also reported. Section 4 presents the study of FLEM in tokamak plasmas with a circular cross section. This allows a more straightforward comparison of the FLEM physics between two different configurations. The summary and a brief discussion are presented in section 5.

2. Models and formulations

2.1. Toroidal self-consistent MHD-kinetic hybrid model

The MARS-K code numerically solves the linearized, single-fluid MHD equations with self-consistent inclusion of drift kinetic resonances in toroidal geometry [18]. For a given curvilinear flux coordinate system (s, χ, φ), and assuming that all the perturbations have the form $A(s, \chi, \varphi, t) = A(s, \chi)\mathrm{e}^{-\mathrm{i}\omega - \mathrm{i}n\varphi}$, the MHD equations are written in the Eulerian frame

$$-\mathrm{i}(\omega - n\Omega)\boldsymbol{\xi} = \mathbf{v} + (\boldsymbol{\xi} \cdot \nabla \Omega)R^2 \nabla \phi \tag{1}$$

$$-\mathrm{i}\rho(\omega - n\Omega)\,\mathbf{v} = -\nabla \cdot \mathbf{p} + \nabla \times \mathbf{Q} \times \mathbf{B} + \nabla \times \mathbf{B} \times \mathbf{Q}$$
$$- \rho\,[2\Omega\widehat{\mathbf{Z}} \times \mathbf{v} + (\mathbf{v} \cdot \nabla \Omega)R^2 \nabla \phi] \tag{2}$$

$$-\mathrm{i}(\omega - n\Omega)\,\mathbf{Q} = \nabla \times (\mathbf{v} \times \mathbf{B}) + (\mathbf{Q} \cdot \nabla \Omega)R^2 \nabla \phi \tag{3}$$

$$\mathbf{p} = p_{\parallel}\widehat{\mathbf{b}}\widehat{\mathbf{b}} + p_{\perp}(\mathbf{I} - \widehat{\mathbf{b}}\widehat{\mathbf{b}}) \tag{4}$$

$$\text{and } p_{\parallel} = \sum_j \int M_j v_{\parallel}^2 f_j^1 \mathrm{d}\Gamma, \; p_{\perp} = \sum_j \int \frac{1}{2}M_j v_{\perp}^2 f_j^1 \mathrm{d}\Gamma \tag{5}$$

where s is the normalized radial coordinate labeling the equilibrium flux surface. χ is a generalized poloidal angle. $\omega = \omega_{\mathrm{r}} + \mathrm{i}\gamma$ is the complex eigenvalue of the mode (γ being the mode growth rate, ω_{r} the mode rotation frequency in the laboratory frame). The mode frequency is corrected by a Doppler shift in Ω, with n being the toroidal mode number, Ω the plasma rotation frequency in the torodial direction ϕ. $\boldsymbol{\xi}$, $\mathbf{v}$, $\mathbf{Q}$, $\mathbf{j}$, $\mathbf{p}$ represent the perturbed quantities: the plasma displacement, the perturbed velocity, magnetic field, current and kinetic pressure tensor, respectively. ρ is the unperturbed plasma density. $\mathbf{B}$ is the equilibrium magnetic field. R is the plasma major radius. $\widehat{\mathbf{Z}}$ is the unit vector in the vertical direction. A conventional unit system is assumed with the vacuum permeability $\mu_0 = 1$; and the subsonic plasma flow is assumed.

The perturbed kinetic pressure tensor $\mathbf{p}$ includes both parallel (to the equilibrium magnetic field), $p_{\parallel}$, and perpendicular, $p_{\perp}$, components. Each component involves both adiabatic (superscript 'a') and non-adiabatic (superscript 'na') parts: $p_{\parallel} = p_{\parallel}^{\mathrm{a}} + p_{\parallel}^{\mathrm{na}}$, $p_{\perp} = p_{\perp}^{\mathrm{a}} + p_{\perp}^{\mathrm{na}}$.

$$p_g^a = \sum_j \int d\Gamma E_g (-\xi_\perp \cdot \nabla f_j^0), \qquad (6)$$

$$p_g^{na} = \sum_j \int d\Gamma E_g f_j^1 \quad g = \parallel, \perp, \qquad (7)$$

where $E_\parallel = M v_\parallel^2$, and $E_\perp = M v_\perp^2 / 2 = \mu B$ (μ is the magnetic moment). $\mathbf{I}$ is the unit tensor, and $\mathbf{b} = \mathbf{B}/|B|$. Γ denotes the velocity space of particles, and j denotes the particle species including thermal ions and electrons as well as energetic ions ($j = i, e, a$). f_j^0 is the equilibrium distribution function. f_j^1, is the solution of the perturbed drift kinetic equation, which we solve together with the fluid equations [19, 20]. Therefore, this self-consistent approach provides a drift kinetic closure to the single-fluid MHD equations. Besides, a set of vacuum equations for the perturbed magnetic field $\mathbf{Q}$, and the resistive wall equation based on the thin-shell approximation, are all solved together with equations (1)–(4) [21].

We assume Maxwellian equilibrium distributions for thermal ions and electrons, and adopt a slowing down distribution for the energetic ions (in what follows, 'EPs' always refers to energetic ions)

$$f_a^0(\psi, \varepsilon_k) = \begin{cases} \dfrac{c(\psi)}{\varepsilon_k^{3/2} + \varepsilon_c^{3/2}} & 0 < \varepsilon_k < \varepsilon_\alpha \\ 0 & \varepsilon_k > \varepsilon_\alpha \end{cases} \qquad (8)$$

where $\varepsilon_c = \left(\frac{3\sqrt{\pi}}{4} \right)^{2/3} \left(\frac{M_a}{M_i} \right) \left(\frac{M_i}{M_e} \right)^{1/3} T_e$, M_i, M_e and M_a denote the mass of thermal ion, electron and energetic ion respectively; The constant ε_α is the so-called birth energy, defined as

$$\varepsilon_\alpha = \begin{cases} 3.5 \, \text{MeV} & \alpha\text{-particles} \\ \varepsilon_\alpha(s) & \text{beam-driven fast ions} \end{cases} \qquad (9)$$

The factor $c(\psi)$ is determined by the EP density $N_a = \int f_a^0 d\Gamma$. Equation (8) is a reasonable model for simulating the fusion born alphas. And within certain approximation, it can be used to model fast ions produced by the neutral beam injection [22].

The drift kinetic effects from each species of particles are self-consistently coupled to MHD equations; the detailed description can be found in [18]. For thermal particles, the key element in this formulation is the wave-particle resonance operator, expressed as

$$\lambda_{ml}^\alpha = \frac{n \left[\omega_{*N} + (\hat\varepsilon_k - 3/2) \omega_{*T} + \Omega \right] - \omega}{n\omega_d + [\alpha(m + nq) + l] \omega_b + n\Omega - \omega - i\nu_{eff}} \qquad (10)$$

where ω_d is the bounce-orbit-averaged precession drift frequency. $\hat\varepsilon_k = \varepsilon/T$ is the particle kinetic energy normalized by the temperature and ν_{eff} is the effective collision frequency. For trapped particles, $\alpha = 0$, and ω_b is the bounce frequency. For passing particles, $\alpha = \pm 1$, and ω_b represents the transit frequency. Similar to thermal particles, the precessional drift resonance operators for fast ions can be expressed as

$$\lambda^a = \frac{n \left(\frac{\partial f_a^0}{\partial \psi} \middle/ \frac{Ze \partial f_a^0}{\partial \varepsilon_k} \right) - \omega}{n\omega_{da} + n\Omega - \omega - i\nu_{eff}} \qquad (11)$$

where ω_{da} is the bounce orbit averaged precessional drift frequency of fast ions. In this work, we shall neglect the finite banana orbit effect, as well as the anisotropy effect associated with the particle pitch angle distribution. These two effects can readily be extended in a future study.

2.2. Quadratic energy terms

In order to gain better physics insight, we shall evaluate various perturbed energy components in the quadratic form [23, 24], for both fluid and drift kinetic contributions. These energy components are evaluated *a posteriori*, based on the self-consistently computed mode eigenfunctions. We define the following energy components of the fluid potential energy δW_F and the kinetic potential energy δW_k.

$$\delta W_F = \delta W_j + \delta W_Q + \delta W_p \qquad (12)$$

where

$$\delta W_j = \frac{1}{2} \int |Q|^2 J ds d\chi d\phi$$

$$\delta W_Q = \frac{1}{2} \int \left[J_\parallel \mathbf{b} \cdot \xi_\perp^* \times \mathbf{Q}_\perp - \frac{Q_\parallel}{B} (\xi_\perp^* \cdot \nabla P) \right] J ds d\chi d\phi$$

$$\delta W_p = \frac{1}{2} \int (\nabla \cdot \mathbf{p}^a) \cdot \xi_\perp^* J ds d\chi d\phi$$

J is the Jacobian of the flux coordinates. The drift kinetic potential energy term is obtained as

$$\delta W_k = \frac{1}{2} \int_{V^P} J ds d\chi d\phi \left[p_\perp^{na} \frac{1}{B} (Q_\parallel^* + \nabla B \cdot \xi_\perp^*) + p_\parallel^{na} \kappa \cdot \xi_\perp^* \right] \qquad (13)$$

Taking into account equation (7), the drift kinetic energy component, contributed from the thermal ion and electrons, can be expressed as [25]

$$\delta W_k^{e,i} = \frac{\nu\sqrt{\pi}}{2B_0} \sum_{e,i} \int d\Psi P_{e,i} \left\{ \int d\hat\varepsilon_k \hat\varepsilon_k^{5/2} e^{-\hat\varepsilon_k} \right.$$
$$\left. \times \sum_\sigma \left[\int d\Lambda \sum_l \lambda_l^\alpha \hat\tau_b \left| \langle e^{-i(l + \alpha nq)\omega_b t - in\phi} H_L^{e,i} \rangle_l \right|^2 \right] \right\} \qquad (14)$$

where Ψ is the equilibrium poloidal flux, $P_{e,i}$ denotes the ion and electron equilibrium pressure, $\Lambda = B_0 \mu / \varepsilon_k$ (B_0 is the on-axis equilibrium magnetic field strength), $\sigma = \text{sign}(v_\parallel)$. The integration is taken in both the real and the velocity spaces. The sum is over the modified bounce harmonics l (which includes the poloidal Fourier harmonics m) and the passing and trapped particles, as well as over the particle species (e, i). For trapped particles, $\alpha = 0, \nu = 1/2$ and $\hat\tau_b$ is the bounce period normalized by a factor $\sqrt{M/2\varepsilon_k}$; for passing particles, $\alpha = \sigma, \nu = 1$ and $\hat\tau_b$ represents the normalized transit period. $\langle \cdot \rangle$ denotes the time average over the bounce/transit period.

The contribution from the trapped EPs (ions) is written as

$$\delta W_k^\alpha = \frac{1}{2} \int d x^3 \int d\Gamma \varepsilon_k \left(-\frac{\partial f_a^0}{\partial \varepsilon_k} \right) \lambda^a \left| \langle e^{in\tilde\phi(t)} H_L^a(t) \rangle \right|^2 \qquad (15)$$

H_L^j is the perturbed particle Lagrangian for each particle species [20]

$$H_L^j(s, \chi, \Lambda) = 2\left(1 - \frac{\Lambda}{h}\right)\boldsymbol{\xi}_\perp \cdot \boldsymbol{\kappa} + \frac{\Lambda}{B_0}(Q_\parallel + \boldsymbol{\xi}_\perp \cdot \nabla B) \quad (16)$$

where $h = B_0/B$. The total drift kinetic energy component is the combination of the contribution from all particle species. $\delta W_k = \sum_j \delta W_k^j$.

In the energy calculations, we neglect the centrifugal and the Coriolis force terms in the RHS of equation (2), assuming a slow (subsonic) equilibrium flow. The vacuum energies, $\delta W_{v\infty}$ and δW_{vb}, without wall and with an ideal wall at the minor radius b, respectively, are written as

$$\delta W_{v\infty} = \frac{1}{2}\int_{V^\infty} |\mathbf{Q}|^2 J \mathrm{d}s \mathrm{d}\chi \mathrm{d}\phi = -\frac{1}{2}\int_{S^p} b_1^n \widehat{V}_1^{*\infty} J_s \mathrm{d}\chi \mathrm{d}\phi \quad (17)$$

$$\delta W_{vb} = \frac{1}{2}\int_{V^b} |\mathbf{Q}|^2 J \mathrm{d}s \mathrm{d}\chi \mathrm{d}\phi = -\frac{1}{2}\int_{S^p} b_1^n \widehat{V}_1^{*b} J_s \mathrm{d}\chi \mathrm{d}\phi \quad (18)$$

where b_1^n is the normal magnetic field perturbation $V_1^{*\infty,b}$ is the complex conjugate of the perturbed magnetic scalar potential, which is determined by the ideal wall position and b_1^n at the plasma surface [24]. In the above calculations, we have assumed cases with vanishing equilibrium pressure at the plasma edge, i.e. $P(a) = 0$.

2.3. The equilibrium profiles of energetic particles

In this study, we denote the density and pressure fractions of EPs, with respect to the bulk thermal particles, by $N^* = N_a/N_e$, and $P^* = P_a/P_{th}$, respectively, where the subscripts 'a', 'e' and 'th' denote the species of EPs ($P_a = \frac{2}{3}\int f^0 \varepsilon_k \mathrm{d}\Gamma \propto N_a \varepsilon_\alpha$), electrons and the bulk thermal particles (ions plus electrons). The total equilibrium plasma pressure is $P_{total} = P_{th} + P_a$. Both N^* and P^* are functions of the plasma minor radius s, which is the coordinate linked to the poloidal magnetic field flux.

Consequently, the beta fraction of EPs is denoted by β^*, $\beta^* = \beta_a/\beta_{th}$. For RFPs, the poloidal beta value β_p is commonly in use, while in tokamaks the total beta value β is usually used. By seeking convenience for the numerical analysis, we consider two types of $P^*(s)$ profiles (normalized by β_0^2/μ_0): (1) $P^*(s) = \beta_0^*$, which is a constant along the minor radius, thus $\beta^* = \beta_0^*$; (2) $P^* = \beta_0^*(1 - s^2)^8$, in which, obviously, the value of β^* appears much smaller than β_0^*. As examples, figure 1 shows the corresponding profiles for type (1) with $\beta^* = \beta_0^* = 0.3$. The equilibrium pressure (*a*) and density profiles (*b*) of the hot ions, bulk thermal particles, and total particles are separately plotted. Figure 2 shows the pressure and density profiles for type (2), with $\beta_0^* = 1.0$ and $\beta^* = 0.176$.

The profiles shown in figure 2 shall be used in most of the computations. Thus, the corresponding results shall be reported without specific mention of this type. The profiles with $\beta^* = \beta_0^* = $ constant, shown in figure 1, are assumed in a few numerical analyses as the simplest test case. The corresponding results will be reported with specific mention of this type in the figure captions. The difference between these two types of profiles does not cause a qualitative change in the nature of the FLEM instability.

3. FLEM in RFP plasmas

In this work, we first discuss FLEM physics in RFP plasmas, because the FLEM instabilities in RFP mainly possess the coupling between non-resonant poloidal harmonics (with the mode's rational surfaces being outside the plasma), thus representing relatively simpler physics. As we shall show, the FLEM instability in tokamak plasmas has essentially a similar nature to that in RFPs, although the (dominant) non-resonant harmonic couples to the resonant ones (with the rational surfaces inside the plasma) in the former. Nevertheless, only marginal differences are obtained between these two different configurations, regarding the EP triggering of FLEM.

3.1. Driving mechanism of FLEM

The RFP magnetic configuration is characterized by the sign change of the toroidal magnetic field profile (so-called 'field reversal'), which allows an RFP to operate in the parameter region where the resonant ideal kink modes appear to be stable, whilst the non-resonant external ideal kink modes can be strongly unstable due to the large plasma current, unless a surrounding perfectly conducting wall is located sufficiently close to the plasma surface [26]. Therefore, the non-resonant external kink modes are the easiest to be excited among the kink mode spectrum in RFP plasmas. The detailed description of the RFP equilibrium parameters used in MARS-K can be found in [27].

It is interesting to note that, in contrast to the RWM, FLEMs satisfy the usual external ideal kink dispersion relation:

$$-\delta I + \delta W_F + \delta W_{vb} + \delta W_k = 0 \quad (19)$$

where δI represents the inertial energy component. The normalized version of equation (19) (by $\int \rho |\xi|^2 \mathrm{d}x^3$) can be further written in real and imaginary parts, separately

$$(n\Omega - \omega_r)^2 - \gamma^2 = \delta W_F^r + \delta W_{vb} + \delta W_k^r = \delta W_b^r + \delta W_k^r \equiv \delta W_{bk}^r \quad (20.1)$$

$$-2\gamma(n\Omega - \omega_r) = \delta W_k^i + \delta W_F^i \quad (20.2)$$

where the superscript 'r' denotes the real part of the energy components and 'i' denotes the imaginary part. In the fluid theory (where $\delta W_k = 0$), $\delta W_b > 0$ indicates the external kink mode being stable with an ideal wall at $r = b$. Thus, $\delta W_b = 0$ sets a stability boundary, beyond which, $\delta W_b < 0$, the ideal wall can no longer stabilize the mode. The value of δW_b depends on the equilibrium parameters of the plasma. For a given current profile, the value of δW_b sensitively depends on the plasma beta value (β_p in RFP) and the wall proximity, expressed by the normalized minor radius of the wall, i.e. $r = b/a$. In fact, $\delta W_b = 0$ corresponds to the so-called 'ideal wall beta limit' in the RWM theory, where the ideal non-resonant external kink modes stay marginally stable with an ideal wall. Furthermore, when the kinetic effects (wave–particle interaction) are taken
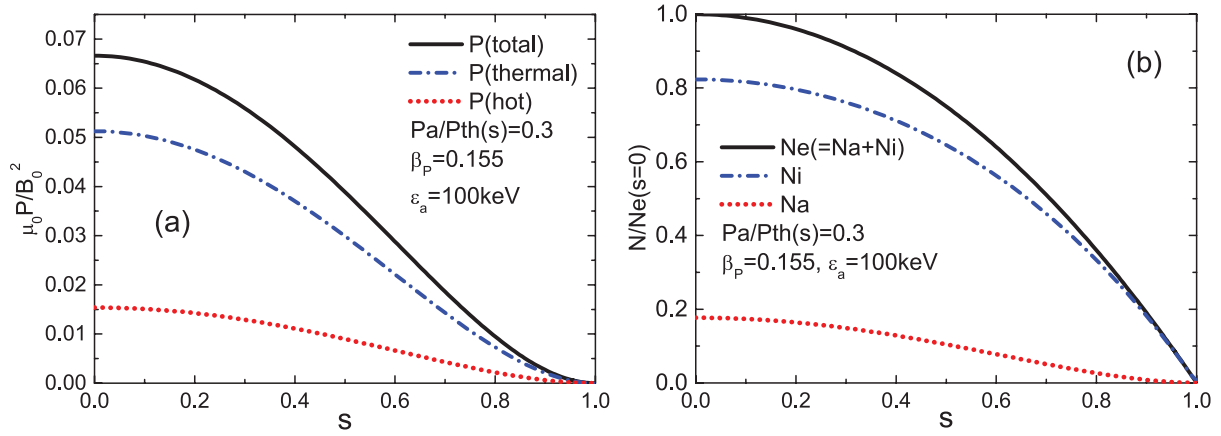
Figure 1. The equilibrium profiles corresponding to the case of $P^* = $ constant: (*a*) the pressure profiles (normalized by B_0^2/μ_0) for hot ions, bulk thermal particles, as well as for all particles; (*b*) the density profiles (normalized by Ne($s = 0$) at the magnetic axis) for thermal ions (N_i) and electrons (N_e), as well as for the energetic ions (N_a). The equilibrium parameters are $P_a/P_{th} = 0.3(\beta^* = \beta_0^* = 0.3)$., $\beta_p = 0.155$, and $\varepsilon_\alpha = 100$ keV.

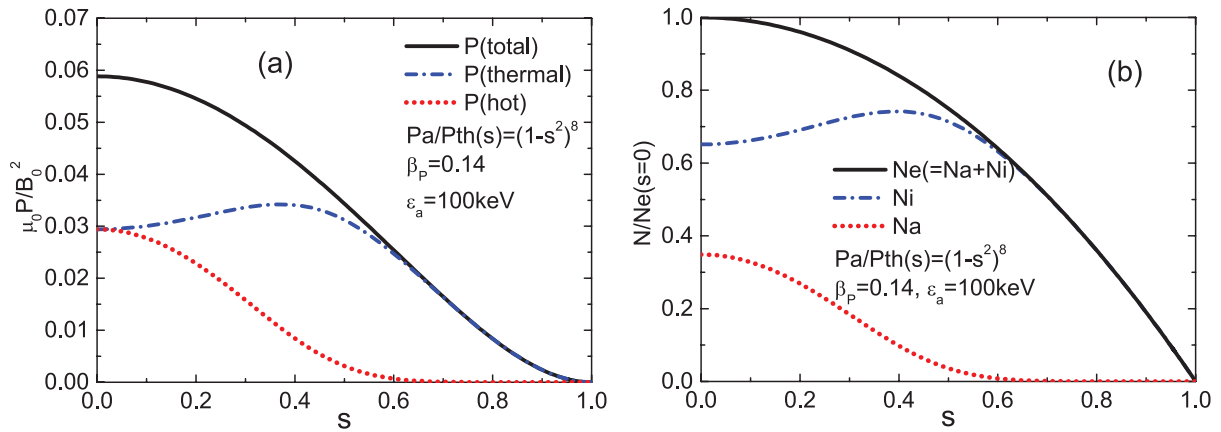**Figure 2.** The equilibrium profiles corresponding to $P*(s) = \beta_0^*(1 - s^2)^8$: (*a*) the pressure profiles (normalized by B_0^2/μ_0) of hot ions, bulk thermal particles, as well as for all particles; and (*b*) the density profiles (normalized by the $N_e(0)$ at the magnetic axis) for thermal ions (N_i) and electrons (N_e), as well as for the energetic ions (N_a). The choice of the parameters is $\beta_p = 0.14$ and $\varepsilon_\alpha = 100$ keV, $\beta^* = 0.176$, ($\beta_0^* = 1.0$).

into account, as shown in equation (20.1), the contribution of the drift kinetic energy component δW_k^r modifies the stability boundary of the ideal kink mode. This will be shown in the following results.

Numerical results show that usually the imaginary part of δW_k is much larger than that of δW_F, i.e. $\delta W_k^i \gg \delta W_F^i$, Therefore, equation (19) can be written as

$$(n\Omega - \omega_r)^2 = \frac{1}{2}\left[\delta W_{bk}^r + \sqrt{(\delta W_{bk}^r)^2 + (\delta W_k^i)^2}\right] \quad (21A)$$

$$\text{and } \gamma = -\frac{\delta W_k^i}{2(n\Omega - \omega_r)} \quad (21B)$$

Moreover, we find that in most parameter regions of RFP plasmas, δW_k^r is the dominant term in δW_{bk}^r, and $\gamma \ll \omega_r$. Equation (20) can thus be further approximated as

$$|n\Omega - \omega_r| \approx \sqrt{\delta W_b^r} \quad (22A)$$

$$\gamma \approx \frac{\delta W_k^i}{2\sqrt{\delta W_b}} \quad (22B)$$

Equations (22A) and (22B) clearly indicate the FLEM physics, that the kink mode frequency is mostly determined by the real part of the energy components δW_b, and the growth rate of the instability is mainly contributed by δW_k^i, which comes from the precessional drift resonance of the trapped energetic ions. If the mode frequency ω_r falls inside a range satisfying the resonant condition with the precessional frequency of a given type of EPs, i.e. $\omega_r - n\Omega \approx n\omega_{da}$, the FLEM instability may occur. Therefore, the FLEM frequency ω_r directly links to the value of ω_{da}, and the plasma rotation provides a Doppler shift $n\Omega$ on the frequency.

Obviously, in the limit case, where the plasma β_p reaches the vicinity of the ideal wall beta limit, $\delta W_{bk} \approx 0$, and δW_k^i play the major role in the dispersion relation. Equation (20) results in
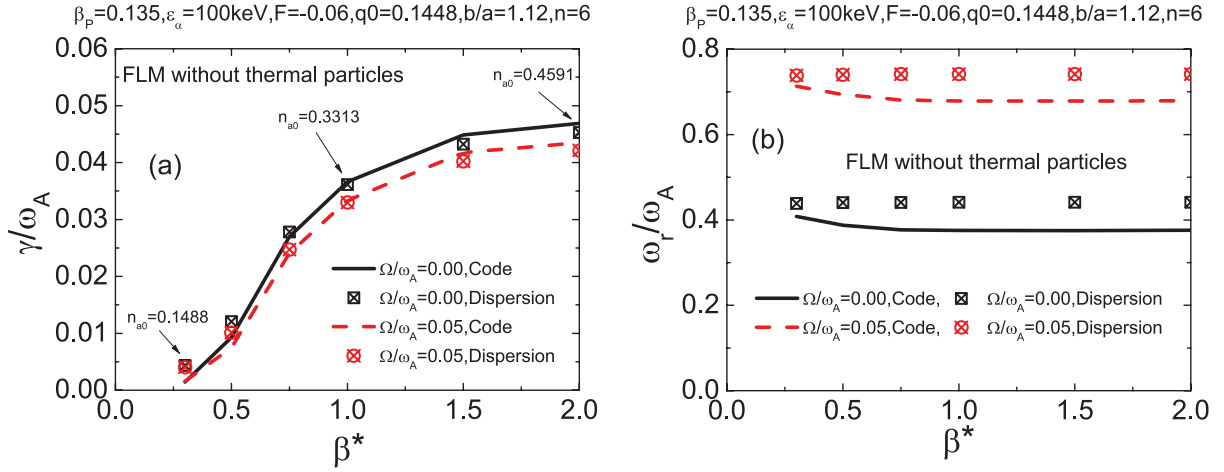
Figure 3. The normalized (*a*) growth rates γ/ω_A, and (*b*) real frequencies ω_r/ω_A, of the FLEM as functions of the beta fraction of EPs $\beta^* = \beta_\alpha/\beta_{thermal}$. Two cases are compared, with $\Omega = 0$ and $\Omega/\Omega_A = 0.05$. Comparisons are also made between the direct MARS-K results (lines) and those by using the dispersion relation (22) (dots). The equilibrium parameters are chosen as: $\beta_p = 0.135$, $b/a = 1.12$, $F = -0.06$, $\varepsilon = a/R = 0.23$, and $q(0) = 0.1448$. F is the reversal parameter in RFP configuration ($F = B\varphi(a)/< B\varphi>$).

$$\gamma \approx |n\Omega - \omega_r| \approx \sqrt{\delta W_k^i/2}. \qquad (23)$$

Figure 3 shows (*a*) the normalized growth rates and (*b*) the frequencies of the MARS-K computed $n = 6$ FLEM instability as a function of β^* in the RFP plasma. Only the kinetic effects from the precessional drift motion of trapped EPs are taken into account in the computations. A comparison has also been made between the results of directly solving the set of equations (1)–(4) by the MARS-K code, and that calculated by using the dispersion relation (22). A good agreement is obtained as presented in the figure. In these plots, both the frequencies and the growth rates are normalized by ω_A, $\omega_A = B_0/(R_0\sqrt{\mu_0\rho_0})$. The birth energy ε_α of hot ions from NBI is taken as $\varepsilon_\alpha = 100$ eV. The EP beta fraction profile is taken as $\beta^* = \beta_0^*$. We fix the total poloidal beta of the plasma at $\beta_p = 0.135$, and vary the β^* value from 0.0 to 2.0 (corresponding to the N^* value changing from 0 to 0.4591). Two cases, without plasma rotation $\Omega = 0$ and with rotation $\Omega/\omega_A = 0.05$, are plotted. It shows that, when β^* exceeds a critical value of $\beta_c^* \approx 0.28$, the FLEM instability appears, at a rather high frequency which is in the range of the Alfven frequency. With an increase in the β^* value, the mode growth rate is enhanced due to the increase in the drift kinetic energy component δW_k^i. Nevertheless, the FLEM frequency remains almost invariant, due to the fact that the value of δW_b remains unchanged. The latter is because the total plasma beta β_p and the wall position b remain the same. Since the birth energy ε_α, and thus ω_{da}, is the same for these two cases (i.e. with and without rotation), the resonance condition of $\omega_r - n\Omega \approx n\omega_{da}$ indicates that the mode has a higher frequency with plasma rotation than the one without, due to the Doppler shift $n\Omega$.

Under our equilibrium assumptions, the value of δW_k^i is mainly determined by two features of EPs: (1) the density fraction of EPs, N_a/N_e, and (2) the birth energy ε_α which directly links to the precession frequency ω_{da}. The parameter $\beta^* (= \beta_\alpha/\beta_{thermal})$ reflects the combination of these two effects. We note here that, in contrast to the RWM theory where δW_k^i
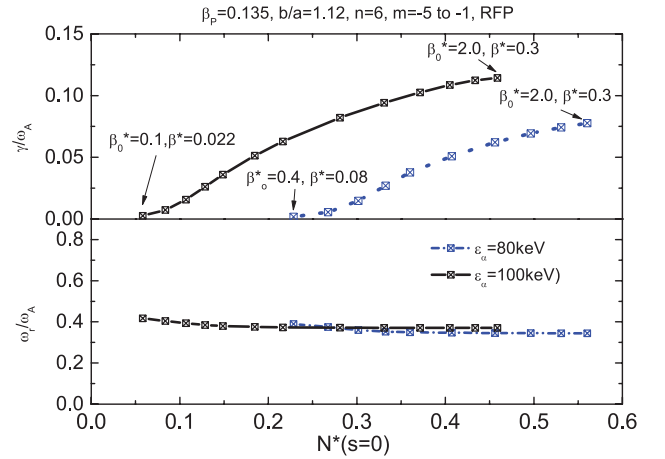

Figure 4. Growth rates and frequencies of the FLEM instability plotted as a function of the density fraction of energetic ions, $N^*(s = 0) = N_a/N_{th}$, for two different birth energies $\varepsilon_\alpha = 80$ keV (dotted lines) and $\varepsilon_\alpha = 100$ keV (solid lines). The values of β^* and β_0^*, corresponding to both ends of the curves, are marked in the figure.

always plays a *stabilizing* role, while the imaginary part of the drift kinetic energy component is the only possible *driven* term for the FLEM instability.

3.2. Excitation conditions of FLEM instability

EPs can induce an unstable external ideal kink mode under two conditions: (1) sufficient fraction of trapped EPs, and (2) the range of the kink mode frequency ω_r can satisfy the resonant condition $\omega_r - n\Omega \approx n\omega_{da}$. For the excitation of FLEM instability, plasma rotation is not necessary, and without rotation $\Omega = 0$, the resonant condition is $\omega_r \approx n\omega_{da}$.

Regarding the first condition, the important measurement is the EP contribution to the imaginary part of the drift kinetic energy component, δW_k^i, as indicated by the dispersion relation (22*B*). Since the value of δW_k^i from EPs is proportional to the EP equilibrium pressure P_a, both the density

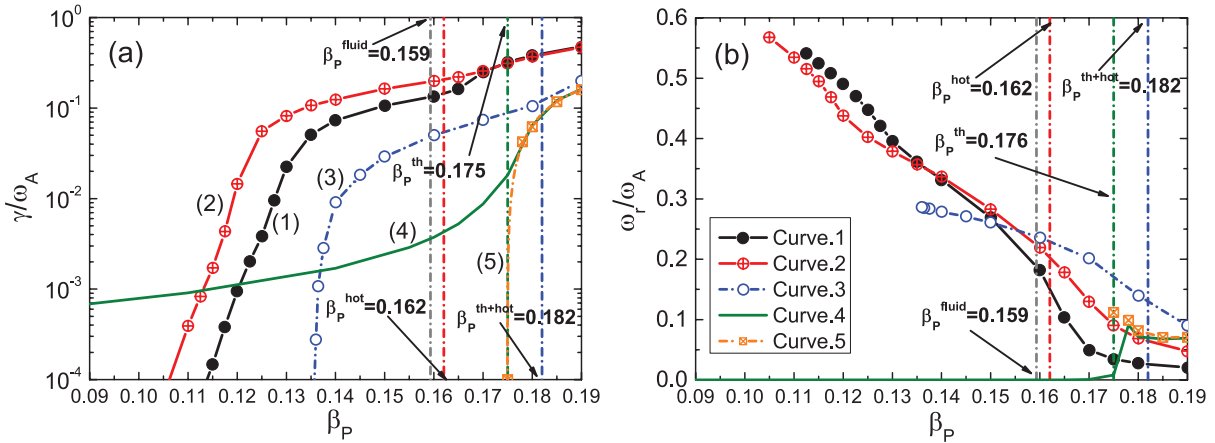**Figure 5.** The (*a*) growth rates, and (*b*) frequencies of the $n = 6$ FLEM instabilities plotted as functions of the plasma poloidal beta β_p, for different β^* values of energetic particles with birth energy $\varepsilon_\alpha = 100$ keV. Comparison is made for five cases: curves (1) and (2) include the kinetic contribution of EPs alone, with $\beta_0^* = 0.3$ ($\beta^* = 0.062$) and $\beta_0^* = 1.0$ ($\beta^* = 0.176$), respectively; Curve (3) includes the kinetic contributions from both EPs and bulk thermal particles, with $\beta_0^* = 1.0$ ($\beta^* = 0.176$); curve (4) and (5) include thermal particles only (no EPs), in the presence of either (4) a resistive wall (penetration time scale $\tau_w/\tau_A = 4.4 \times 10^3$), or (5) an ideal wall. The other parameters are $b/a = 1.12$, $F = -0.06$, $q_0 = 0.1448$ and $\Omega = 0$.

fraction N_a^* and the birth energy ε_α can influence δW_k^i via P_a. The birth energy ε_α is even more important, since it directly relates to the EP precession frequency ω_{da}, thus sensitively affecting the resonant condition and consequently the kinetic resonant energy component δW_k^i. These are confirmed by self-consistent numerical results. Figure 4 shows the normalized mode growth rates and frequencies versus the density fraction of EPs for two different birth energies $\varepsilon_\alpha = 100$ keV and $\varepsilon_\alpha = 80$ keV. Energetic ions with higher birth energy drive FLEM instability at much lower critical β^* value and lower density fraction. For the same β^* value, higher birth energy leads to higher growth rate. The mode frequencies are almost the same for the two cases, due to the same β_p value for the two ε_α cases.

The total plasma beta value significantly influences the behavior of FLEM, as shown by figure 5, where we plot (*a*) the growth rates, and (*b*) the frequencies, of FLEM as a function of the total plasma poloidal beta β_p, for the birth energy of $\varepsilon_\alpha = 100$ keV and without plasma rotation. Four different cases of the kinetic resonant contributions are compared: (1) hot ions only, with $\beta_0^* = 0.3$ ($\beta^* = 0.062$) (2) hot ions only, but with higher EP fraction $\beta_0^* = 1.0$ ($\beta^* = 0.176$), (3) both hot ions and bulk thermal particles, with $\beta_0^* = 1.0$ ($\beta^* = 0.176$), (4) thermal particles alone (without hot ions). In the latter case (4), the FLEM is not triggered. Only an unstable RWM is computed by assuming a resistive wall (curve (4) in figure 5), or alternatively an unstable ideal kink is found by assuming an ideal wall, at the value β_p exceeding the ideal wall beta limit, β_p^{ideal} (curve (5) in figure 5). Comparison between cases (1) and (2) shows that EPs with higher β^* (implying higher density fraction N^*) drive FLEM instability in a wider region in β_p, and with higher growth rates. By including the kinetic contributions from bulk thermal particles, as in case (3), the unstable domain for FLEM shrinks, due to a cancellation effect of the kinetic contributions to δW_k^i, between the driving term due to the precession resonance of EPs, and the damping

term due to the transit resonance of thermal particles (mainly ions). In other words, the ion acoustic Landau damping by thermal ions plays a stabilizing role on FLEM.

The upper-bound of the FLEM instability window appears in the region $\beta_p \approx \beta_p^{ideal}$ ($\beta_p \lesssim \beta_p^{ideal}$), where the external kink mode is close to the ideal wall marginal stability point, and the mode has lower frequency resulting from smaller δW_b. For fixed EP parameters (β^*, ε_α), as β_p decreases, the amplitude of the fluid potential energy component $|\delta W_F|$ ($\delta W_F < 0$) decreases, due to the reduction of the pressure-driven effects. This leads to a larger δW_b ($\delta W_b = \delta W_F + \delta W_{vb}$, $\delta W_{vb} > 0$), and thus a higher mode frequency ω_r. As β_p drops down sufficiently low, ω_r becomes too high to satisfy the resonance condition, and EPs can no longer provide sufficient driving energy δW_k^i to trigger the FLEM.

The vertical lines in figure 5 represent the ideal wall beta limits for various aforementioned cases. The drift kinetic contribution modifies the ideal wall beta limit as that predicted by the fluid theory, as has also been observed in experiments [28]. Figure 5 shows that the ideal wall beta limit, β_p^{ideal}, is substantially modified by various kinetic effects. As marked in the figure, the fluid theory predicts the minimum value of $\beta_p^{ideal} = \beta_p^{fluid} = 0.159$ (corresponding to $\delta W_b = 0$); the kinetic effects from EPs alone shift the value to $\beta_p^{ideal} = \beta_p^{hot} = 0.162$ (corresponding to $\delta W_{bk} = 0$); the contribution of thermal particles alone shifts the value to $\beta_p^{ideal} = \beta_p^{th} = 0.175$; finally the combined kinetic effects from both hot ions and thermal particles give the maximum value of $\beta_p^{ideal} = \beta_p^{th+hot} = 0.182$.

Figure 6 presents the radial profiles of various drift frequencies, averaged over the poloidal angle as well as over the particle velocity space, for the case of curve (3) from figure 5. The precession frequency of EPs, and the transit frequencies of thermal ions for three different β_p values ($\beta_p = 0.14, 0.16, 0.18$), are compared. The shaded area indicates the frequency range that corresponds to the full unstable

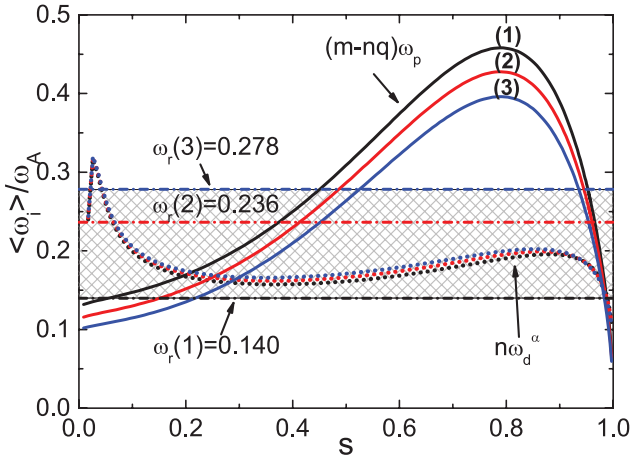**Figure 6.** The precession frequencies of energetic ions, ω_{da}, and the transit frequency of the thermal ions, $(m - nq)\omega_p$, at different β_p values: $\beta_p = 0.18(1), 0.16(2), 0.14(3)$, are shown for the RFP plasma. Compared are also the FLEM frequencies. The shaded area presents the frequency range for the unstable FLEM, as shown by curve (3) in figure 5, where the kinetic effects of both EPs and thermal particles are included.
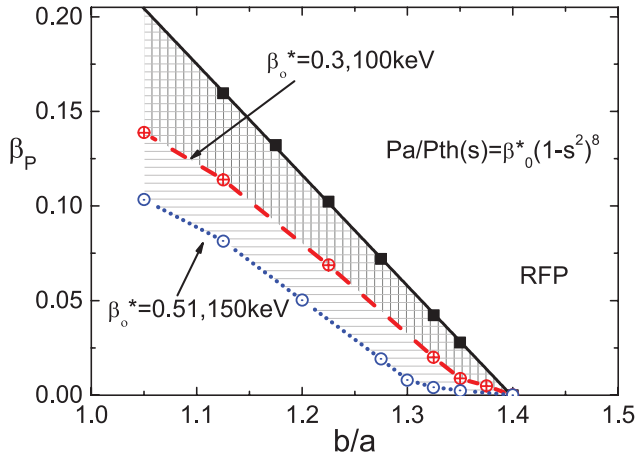

Figure 7. The unstable domain (shaded area) for the $n = 6$ FLEM plotted in the 2D plane of the poloidal beta β_p versus the wall position b/a. The solid line with square points represents the ideal wall beta limit, which is also the upper-bound of the beta value for the FLEM instability. The other two lines (dashed and dotted) represent the lower-bounds of the instability window for the two cases: $\beta_0^* = 0.3$, $\varepsilon_\alpha = 100\,\text{keV}$; and $\beta_0^* = 0.51$, $\varepsilon_\alpha = 150\,\text{keV}$, respectively The other equilibrium parameters are $F = -0.06$, $q_0 = 0.1448$, and $\Omega = 0$.

region of curve (3) in figure 5. Figure 6 thus confirms that both the precession resonance of EPs and the transit resonance of thermal ions can simultaneously occur, which in turn determines the condition for triggering the FLEM.

Figure 7 shows the unstable domain (the shaded area) of the $n = 6$ FLEM in the β_p-b/a plane, for two different choices of the birth energy of EPs. The solid (black) line represents the ideal wall beta limit, whilst the dashed (red) line ($\varepsilon_\alpha = 100\,\text{keV}$) and the dotted (blue) line ($\varepsilon_\alpha = 150\,\text{keV}$) represent the lower-bounds of the unstable domain. No plasma rotation is considered. The higher β^* value (higher birth energy ε_α in this case) results in a larger unstable domain. At a fixed wall

position, the FLEM cannot be triggered at too low a beta. Conversely, at a fixed beta value, the FLEM cannot be triggered if the wall is located too close to the plasma (i.e. too strong a wall stabilization). More detailed discussion of the wall effect is carried out in the next sub-section.

3.3. The role of the surrounding wall on the FLEM instability

Since the FLEM instability has rather high frequency, the usually realistic resistive wall in experiments plays the role of an ideal wall for the FLEM. In fact, our numerical results show that the instability appears independent from the wall resistivity, in most resistivity ranges. For an extremely high resistive wall, the FLEM may couple to the branch of the no-wall ideal kink instability. On the other hand, the radial position of the wall can strongly influence the FLEM triggering, as already shown in figure 7. Figure 8 plots the mode growth rates and frequencies as a function of the wall position b/a, for different choices of the EP birth energies ε_α and the plasma poloidal beta values β_p. Comparisons are also made between a resistive wall (dots) and an ideal wall (lines) assumptions. For the resistive wall, the normalized penetration time is assumed to be $\tau_w/\tau_A = 4.4 \times 10^3$.

The ideal wall and the resistive wall give almost the same results. On the other hand, a wall closer to the plasma sets a more severe condition for the FLEM excitation. In the lower β_p case, with $\beta_p = 0.1$, the ranges of the wall position for the FLEM instability are $b/a = 1.16$–1.225 for $\varepsilon_\alpha = 100\,\text{keV}$, and $b/a = 1.05$–1.225 for $\varepsilon_\alpha = 150\,\text{keV}$. Obviously, EPs with higher ε_α extend the instability to smaller b/a. At even higher β_p, $\beta_p = 0.135$, the instability region of b/a extends to the vicinity of the plasma surface.

3.4. Kinetic effects of thermal particles on FLEMs

The kinetic effects of thermal particles play a stabilizing role on the FLEM instability, as has already been shown by curve (3) of figure 5. By including the kinetic effects of thermal particles, the instability requires higher β_p value, and growth rates are smaller, compared to those of EPs alone. This damping effect is mainly contributed by the transit resonance of passing ions. As shown in figure 6, the transit frequency of passing ions is comparable to the precession frequency of EPs; and both can be in resonance with the FLEM. On the other hand, it turns out that a cancellation occurs between the thermal and the energetic ion contributions to the imaginary part of the drift kinetic energy component. As a result, thermal particles play a damping role on the FLEM instability. This cancellation effect is shown in figure 9, where various perturbed energy components (normalized by $\int \rho |\xi|^2 \, dx^3$) are computed at $\beta_p = 0.14$ (see figure 5). Two cases—with and without thermal particles—are compared for the same β^* value, $\beta^* = 1.0$. In the first group of the energy columns, only the kinetic contribution of hot ions is considered (corresponding to case (2) in figure 5). In the second group, contributions from both hot ions and thermal particles are included (corresponding to case (3) in figure 5). In each group, the
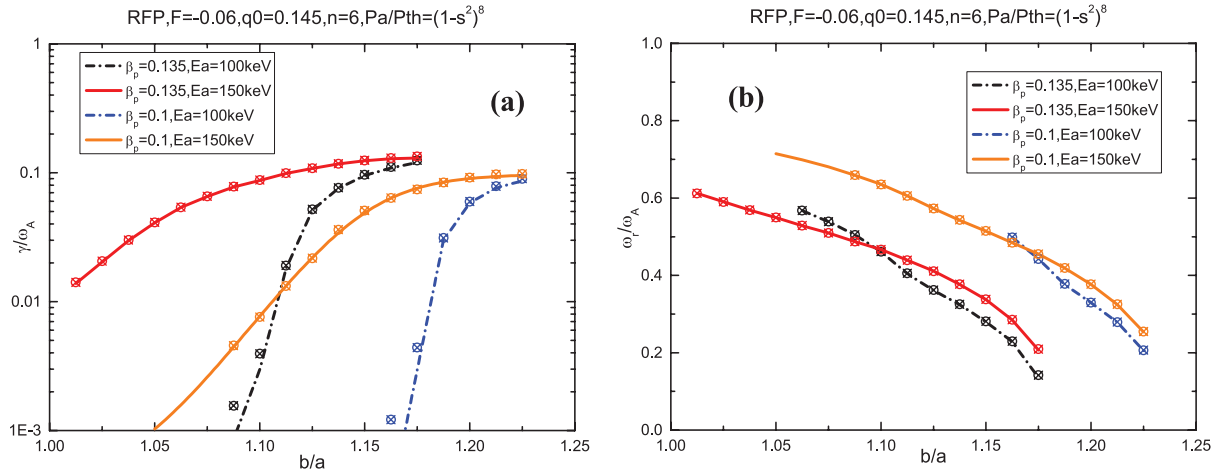
Figure 8. The MARS-K computed (*a*) growth rates and (*b*) frequencies of the $n = 6$ FLEM instability versus the normalized wall position b/a. The lines represent results with an ideal wall, and the dots represent results with a resistive wall having a penetration time of $\tau_w/\tau_A = 4.4 \times 10^3$. The other parameters are the same as those in figure 7.
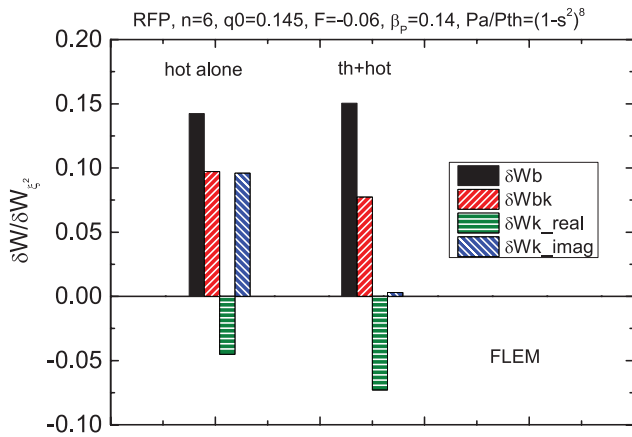

Figure 9. Comparison of the energy components between two groups: the first group represents results with kinetic effects of hot ions alone; the second group includes the kinetic contributions from both hot ions and the full kinetic resonances with thermal particles. The other parameters used here are the same as those in figure 5, at $\beta_p = 0.14$ and $\beta_0^* = 1.0$.

first column represents the fluid contribution δW_b, the second column is $\delta W_{bk} = \delta W_b + \delta W_k^r$, the third one is δW_k^r, and the fourth is the imaginary part of kinetic energy δW_k^i. The value of δW_k^i in the second group drastically decreases with respect to the first group due to the cancelation effect, whilst the other components experience only minor changes. Furthermore, it can be easily understood why the mode frequency becomes slightly lower with the inclusion of thermal particles—this is essentially due to the modification brought by δW_k^r to δW_b, ($\delta W_{bk} < \delta W_b$).

Figure 10 further demonstrates this cancellation effect, by plotting (*a*) the imaginary, and (*b*) the real, part of the drift kinetic energy component with varying plasma toroidal beta β_p (see curves (3) of figure 5). Figure 10(*a*) shows that significant cancelation occurs in the whole unstable region, for the imaginary part δW_k^i, implying that the ion Landau damping by thermal particles plays a stabilizing role for the FLEM instabilities. Figure 10(*b*) shows that the kinetic contribution to

the real part δW_k^r, provided by thermal particles, also slightly modifies (cancels) that by energetic ions, resulting in a modification of the mode frequency.

3.5. Relation with the RWM

The fish-bone-like external kink mode can co-exist and/or couple with the resistive wall mode. Both modes originate from the ideal external kink, which is stable in the plasma with a sufficiently close-fitting ideal wall. The RWM instability is introduced by the replacement of the ideal wall with a resistive wall, which allows the penetration of the perturbed magnetic field; whilst the FLEM instability is driven by the precession motion of trapped EPs, which resonate with the external kink mode.

Figure 11 shows the normalized mode growth rates γ/ω_A and frequencies ω_r/ω_A, for both FLEMs and RWMs, as functions of the plasma rotation frequency Ω/ω_A, for various β^* values of EPs. The beta value of thermal particles remains invariant $\beta_{\text{thermal}} = 0.015$. The kinetic contribution from hot ions alone is included here. Panel (*a*) shows the negative rotation ($\Omega < 0$) case, where the Doppler shift reduces the FLEM frequency. With a further increase in $|\Omega|$, the FLEM frequency ω_r crosses zero (in the vicinity of the RWM frequency), becoming negative. The FLEM remains unstable as the plasma rotation increases, because the resonance condition $\omega_r - n\Omega \approx n\omega_{da}$ is satisfied. The RWM instabilities, instead, are damped by the same motion of hot ions, and become stable with negative rotation, where the similar resonance condition $\omega_r - n\Omega - n\omega_{da} \approx 0$ is satisfied, but with $\omega_r \approx 0$ for the RWM. This figure shows two unstable modes (FLEM and RWM) that generally co-exist. In the particular situation of $\beta^* = 2.13$, $\beta_p = 0.04$, and at rotation $\Omega/\omega_A \approx -0.047$, coupling between the two modes appears, since both frequencies and growth rates of these two modes become very close to each other.

With positive rotation as presented in panel (*b*), the FLEM frequency ω_r stays positive and rapidly increases with rotation, due to the Doppler shift, and thus does not vanish. The RWM,
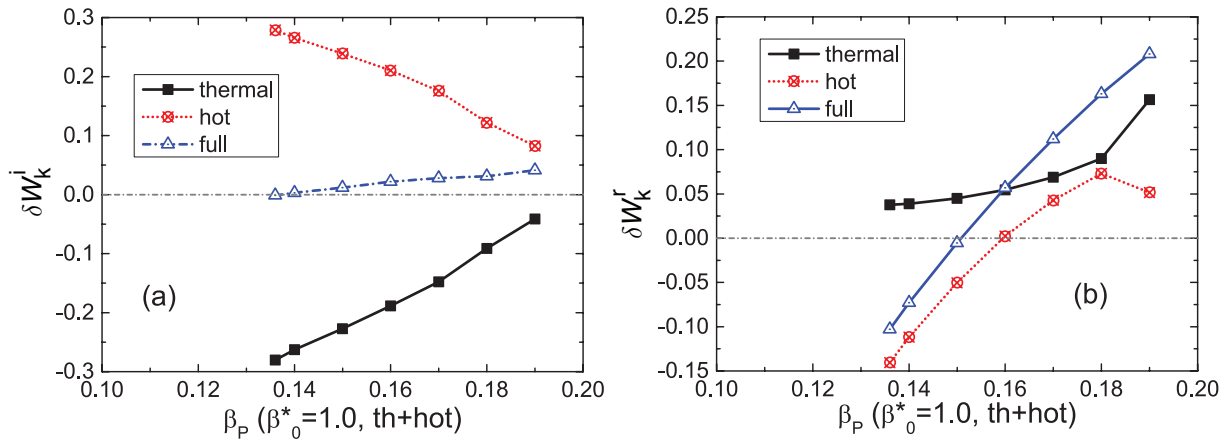
Figure 10. The drift kinetic energy components δW_k versus the poloidal plasma beta β_p, computed at $\beta_0^* = 1.0$, $\beta^* = 0.176$, corresponding to the case (3) of figure 5. Considered are three cases: drift kinetic energy component contributed from the hot ions (marked 'hot'), from the thermal particles (marked 'thermal'), and a combination of both hot and thermal,(marked 'full'). Both (*a*) the imaginary part, and (*b*) the real part, of δW_k, are shown. The other parameters are the same as those in figure 5.
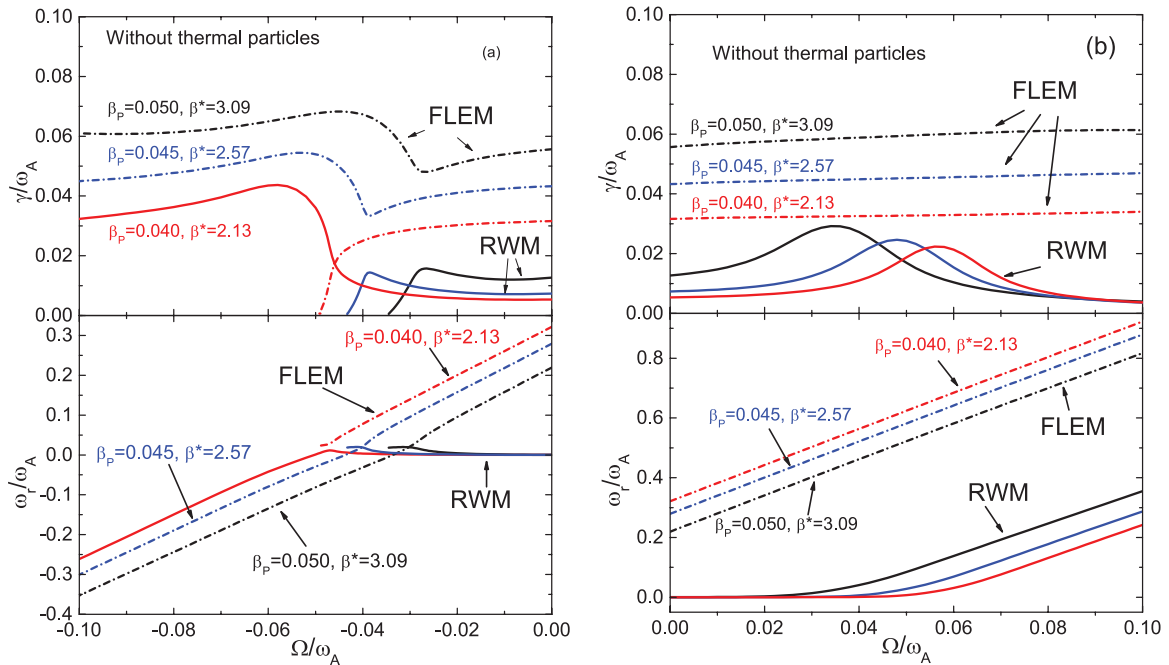

Figure 11. The normalized growth rates and frequencies of the $n = 6$ co-existing and/or coupled RWM and FLEM, plotted as functions of the normalized plasma rotation frequency Ω/ω_A, for $\beta^* = 3.1$ ($\beta_p = 0.05$), $\beta^* = 2.6$ ($\beta_p = 0.045$) and $\beta^* = 2.1$ ($\beta_p = 0.04$), respectively, and with a fixed thermal poloidal beta $\beta_{thermal} = 0.015$. The other choice of parameters is: $\beta^* = $ constant, $b/a = 1.275$, $\varepsilon_\alpha = 100$ keV, $F = -0.015$, and $q(0) = 0.145$.

on the other hand, cannot be stabilized by the kinetic effects of EPs alone—full stabilization can be reached though, if the ion acoustic continuum damping from thermal particles is taken into account [28]. Coupling between the FLEM and the RWM is not observed with positive rotation, due to the large difference in both the mode frequencies and growth rates. Only the co-existence of two modes is presented.

Figure 12 compares the computed eigenfunctions of the FLEM and the RWM, with inclusion of the hot ion kinetic contribution only. The quantity ξ_1 denotes the associated plasma radial displacement, and Q_1 the radial component of the perturbed magnetic field. The example is chosen at $\beta_0^* = 1.0$,

$\beta_p = 0.12$, and without rotation. The penetration time scale of the wall is taken as $\tau_w/\tau_A = 4.4 \cdot 10^3$. Clearly, these two modes, both originated from the 'external kink', have rather similar shapes of the eigenfunctions, for both ξ_1 and Q_1. Nevertheless, a subtle difference can be noticed, both ξ_1 and Q_1 of the FLEM are pushed towards the plasma core by the wall. In particular, Q_1 of the FLEM is nearly vanishing at the wall radius, whilst the RWM field perturbation penetrates well through the wall and extends into the outer vacuum region. Thus, the wall acts as a resistive wall for the RWM (with the mode frequency $\omega_r/\omega_A \approx 0$) but appears as an ideal wall for the FLEM (with $\omega_r/\omega_A \approx 0.48$).
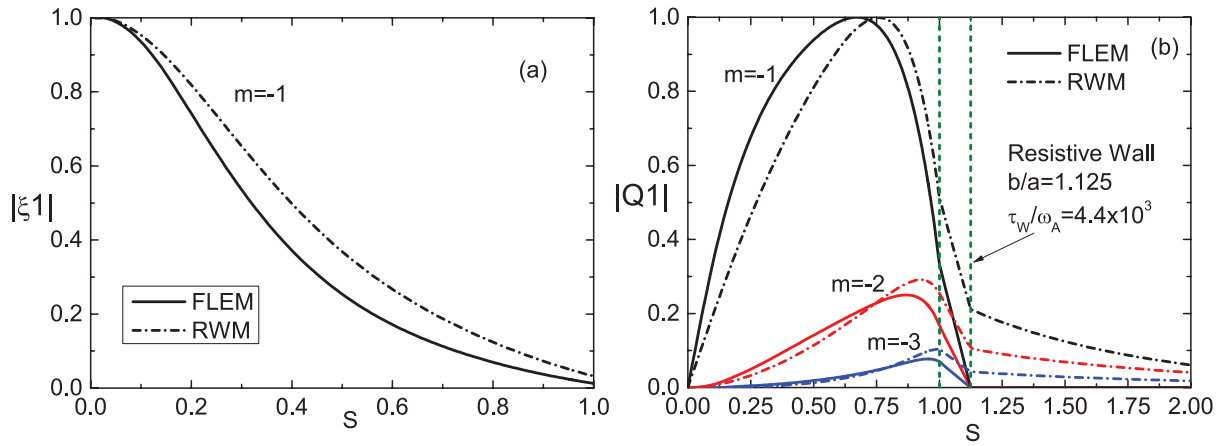
Figure 12. The magnitude of the dominant components of (*a*) the radial plasma displacement $|\xi_1|$ ($n = 6$, $m = -1$) and (*b*) the perturbed radial magnetic field $|Q_1|$ ($n = 6$, $m = -1, -2, -3$), plotted along the minor radius, for both the FLEM and the RWM. The $s = 1$ value corresponds to the plasma surface. The wall is located at $b/a = 1.125$. Included are kinetic effects from hot ions alone. No plasma rotation is assumed. $\beta_0^* = 1.0$, $\beta_p = 0.12$. The other parameters are chosen as the same as those in figure 5.
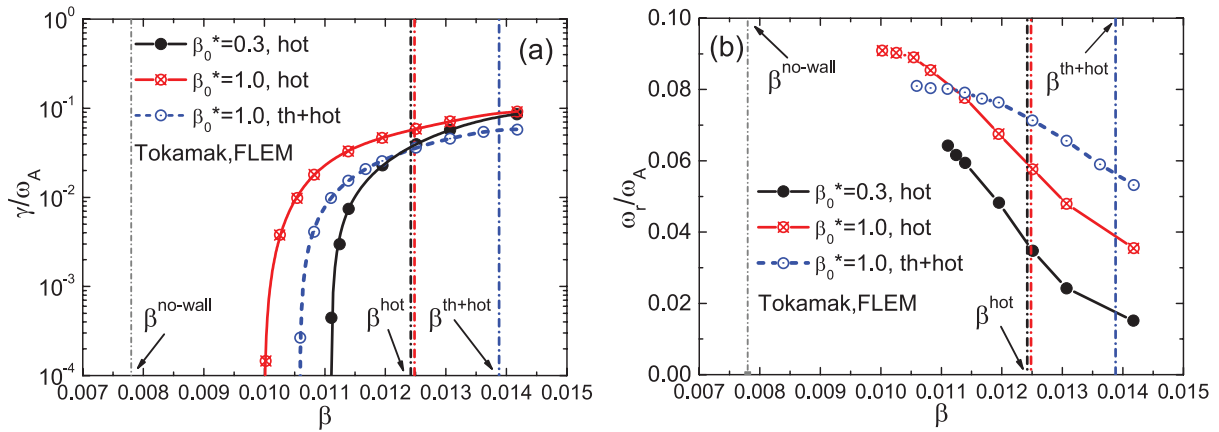

Figure 13. The (*a*) growth rate γ/ω_A, and (*b*) real frequency ω_r/ω_A, of the $n = 1$ FLEM versus the plasma beta β value for the tokamak configuration. The solid lines represent the kinetic contributions from EPs alone, with two different fractions $\beta_0^* = 0.3$ ($\beta^* = 0.067$) and $\beta_0^* = 1.0$ ($\beta^* = 0.19$), respectively. The dashed line represents results with kinetic contributions from both EPs and thermal ions, with $\beta_0^* = 1.0$ ($\beta^* = 0.19$). The other parameters are $b/a = 1.12$, $\Omega = 0$ and $\varepsilon_\alpha = 100$ keV.

4. The FLEM instability in tokamaks

4.1. Excitation of the FLEM instability

The FLEM in the tokamak configuration can be driven by the same mechanism as that in RFPs. Indeed the modes show a similar nature. One difference, though, is that the EP-driven FLEM has much lower frequency in tokamaks, than that in RFPs (with the same birth energy ε_α of EPs). This is because the tokamak configuration has a larger scale length of magnetic gradient and curvature radius (in the order of the major radius R) than that in the RFP configuration (in the order of the minor radius r), resulting in a much lower precession frequency of hot ions in tokamaks than in RFPs. Furthermore, the ion acoustic Landau damping by bulk thermal ions in RFPs would be relatively stronger than in tokamaks, due to the shorter connection length in the former.

Figure 13 shows the growth rates and frequencies of the $n = 1$ FLEM instability versus the total plasma beta β, computed for a circular tokamak equilibrium (such a choice of the plasma shape is mainly motivated by matching the RFP

plasma studied in section 3) with $q(0) = 1.14$, $q(a) = 3.68$, and $b/a = 1.12$. The poloidal harmonics are included from $m = -10$ to 5. The equilibrium parameters of the energetic ions, with $\varepsilon_\alpha = 100$ keV, are assumed to be similar to those shown in figure 5. Three cases are considered: (1) $\beta_0^* = 0.3$ ($\beta^* = 0.067$) and (2) $\beta_0^* = 1.0$ ($\beta^* = 0.19$), where the kinetic effects of EPs alone are included; case (3) $\beta_0^* = 1.0$ ($\beta^* = 0.19$), where the kinetic resonances from both EPs and bulk thermal particles are taken into account. Figure 13 shows similar behavior of the FLEM instability to that shown in figure 5 for RFPs. Namely, the FLEM can also be triggered by EPs in a tokamak configuration, when the plasma beta β exceeds a critical value, which in turn depends on the EP pressure fraction (β^*). Comparison between case (1) $\beta_0^* = 0.3$ and (2) $\beta_0^* = 1.0$ indicates that, the higher the fraction of EPs, the lower the critical β value, and the higher the mode growth rate. The real frequency ω_r/ω_A of the FLEM, which links to the precession frequency of EPs, is also reduced with increasing the plasma beta. Note that the mode frequency ω_r is much lower compared to that in RFPs. The thermal ion Landau
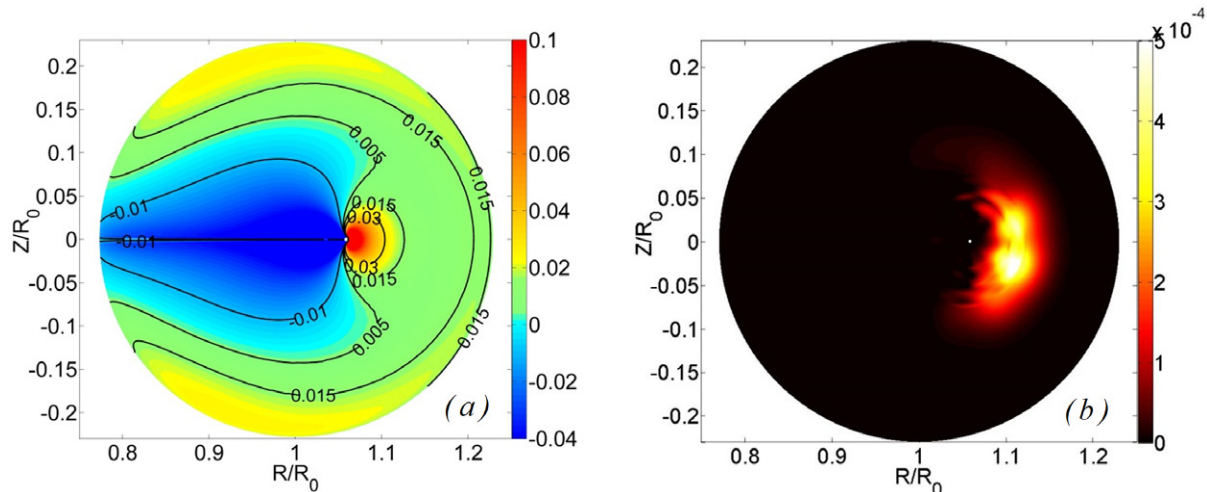
Figure 14. The 2D plots of (*a*) the precession frequency of the EPs $n\omega_{\mathrm{da}}$ (averaged over the particle velocity space), and (*b*) the imaginary part of the drift kinetic energy component $\delta W_{\mathrm{k}}^{\mathrm{i}}$ for the FLEM, with the plasma beta $\beta = 0.012$ ($\beta_N = 3.02$) and the fraction $\beta_0^* = 1.0$ ($\beta^* = 0.19$), are shown in the *R-Z* plane. The other equilibrium parameters are chosen as the same as those from figure 13.

damping also plays a stabilizing role, as can be observed by comparing case (2) (kinetic effects of hot ions alone) and case (3) (kinetic effects of hot plus thermal ions). In tokamaks, the poloidal harmonics of FLEM can be non-resonant and/or resonant. In our case, the dominant non-resonant kink component (e.g. $m = -1$, $n = 1$) couples with the resonant external kink components (e.g. $m = -2, -3$, $n = 1$).

Similar to the RFP case (figure 5), the ideal wall beta limit is modified by the kinetic effects, as marked in figure 13: $\beta^{\mathrm{ideal}} = 0.0124$ ($\beta_N \approx 3.34$) with the EP kinetic effect alone, and $\beta^{\mathrm{ideal}} = 0.0139$ with full kinetic effects (both EPs and thermal ions). The computed no-wall β limit for this plasma is $\beta^{\mathrm{nowall}} = 0.0078$ ($\beta_N^{\mathrm{nowall}} = 2.11$). Here β_N is defined as $\beta_N = \beta_{\mathrm{T}}(aB_{\mathrm{T}}/I)$, $\beta_{\mathrm{T}} = 2\mu_0 <p>/B_{\mathrm{T}}^2$, $<p>$ is the volume averaged plasma pressure, μ_0 is the vacuum permeability and B_{T} is the strength of the toroidal magnetic field.

The general dispersion relation for the external kink mode, equation (21), still applies to the tokamak case. However, the dispersion relation (22), that is valid under the assumption of $\omega_{\mathrm{r}} \gg \gamma$, no longer applies, since ω_{r} is comparable to γ in tokamaks. Thus, the drift kinetic energy component δW_{k} introduces an additional influence on the mode frequency ω_{r}.

The 2D plot in figure 14(*a*) shows the precession frequency $n\omega_{\mathrm{da}}$ (averaged over the velocity space) of EPs. The 2D plot in figure 14(*b*) shows the imaginary part of the drift kinetic energy $\delta W_{\mathrm{k}}^{\mathrm{i}}$ for the FLEM in our tokamak plasma. The kinetic effects of hot ions alone are included here. The other parameters are chosen as $\beta = 0.012$ ($\beta_N = 3.02$), $\beta_0^* = 1.0$, and $\beta^* = 0.19$, corresponding to one of the points in case (2) of figure 13. Figure 14(*b*) shows that the main contribution to the drift kinetic energy $\delta W_{\mathrm{k}}^{\mathrm{i}}$ comes from the region close to the low field side of the magnetic axis, corresponding to the area of $n\omega_{\mathrm{da}} \approx 0.015$–$0.06$ in (*a*), which is also in the vicinity of the FLEM frequency $\omega_{\mathrm{r}}/\omega_{\mathrm{A}} \approx 0.065$ as shown in figure 13 for $\beta = 0.012$. Thus, $\delta W_{\mathrm{k}}^{\mathrm{i}}$ is mainly contributed by the interaction of EPs with the external kink through the precession resonance. We also notice that the values of $n\omega_{\mathrm{da}}$, that provide
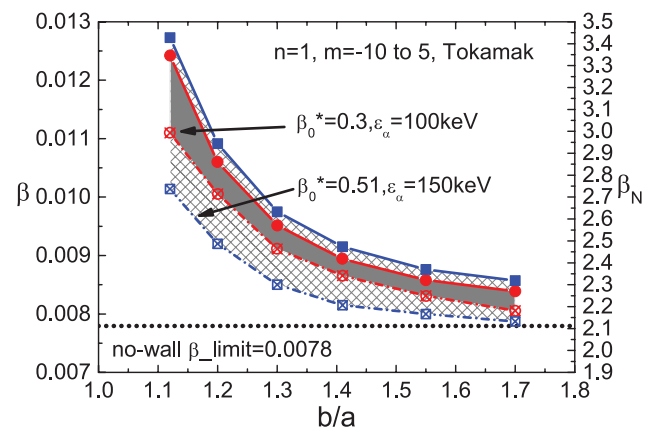

Figure 15. The unstable domains (shaded areas) for the $n = 1$ FLEM, plotted in the 2D plane of the plasma beta β (left) and β_N (right) versus the wall position b/a. The horizontal dashed line represents the no-wall beta limit ($\beta^{\mathrm{nowall}} = 0.0078$). Two different EP parameters are compared: $\beta_0^* = 0.3$ ($\beta^* = 0.067$), $\varepsilon_\alpha = 100$ keV, and $\beta_0^* = 0.51$ ($\beta^* = 0.107$), $\varepsilon_\alpha = 150$ keV. In both cases, the solid lines denote the ideal wall beta limit modified by the kinetic effect, and the dashed lines denote the stability boundary of the FLEMs. No plasma rotation is assumed.

the maximum contribution to the drift kinetic energy $\delta W_{\mathrm{k}}^{\mathrm{i}}$, do not fully coincide with the mode frequency ω_{r}. This discrepancy may be due to the fact that the $n\omega_{\mathrm{da}}$ frequency shown in figure 14(*a*) is the average over the velocity space, whilst the true precessional drift frequency entering into the computations is located in the particle velocity space.

The unstable domains, in the 2D plane of the total plasma β versus the wall position b/a, are mapped out in figure 15 for the $n = 1$ FLEM, for two choices of the parameter set, $\beta_0^* = 0.3$ ($\beta^* = 0.067$) $\varepsilon_\alpha = 100$ keV and $\beta_0^* = 0.51$ ($\beta^* = 0.107$), $\varepsilon_\alpha = 150$ keV, respectively. The unstable (shaded) area appears above the no-wall beta limit (marked in figure 15 as $\beta^{\mathrm{nowall}} = 0.0078$) and below the ideal wall beta limit. The latter is the upper-bound of the unstable region. The EPs with higher birth energy, and/or higher fraction β^*, lead to a larger
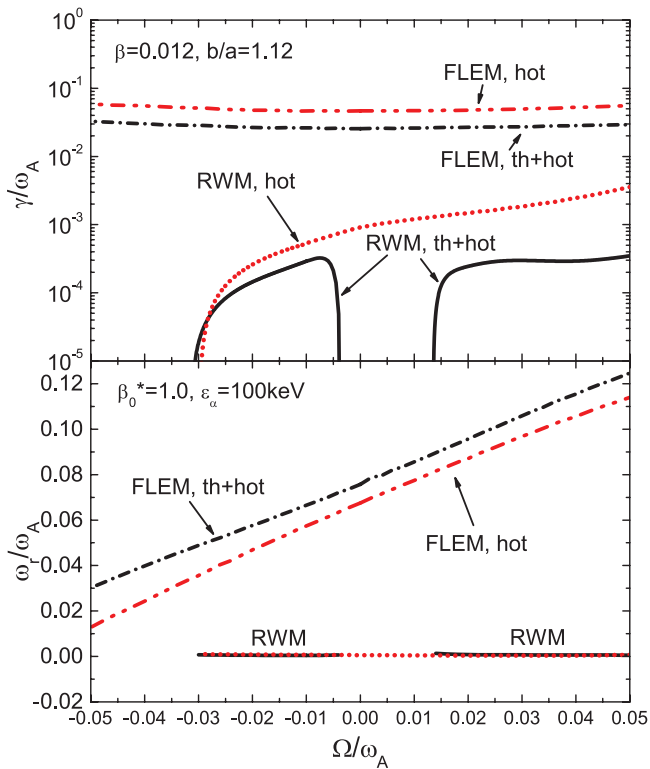
Figure 16. The normalized growth rates and frequencies of the co-existing RWM and FLEM, plotted as functions of the plasma rotation frequency. The mark 'hot' denotes the case where the kinetic effects are contributed only by hot ions; 'th + hot' denotes both hot ions and trapped thermal particles. The other parameters are $\beta_0^* = 1, 0$ ($\beta^* = 0.19$), $\beta = 0.012$, $b/a = 1.12$ and $\varepsilon_\alpha = 100$ keV.

unstable area. Plasma with a closer surrounding wall requires higher beta value to excite the FLEMs. The figure also indicates that the kinetic effects modify the ideal wall beta limit, and hence the upper-bound of the unstable region. Above this limit, the ideal kink mode is intrinsically unstable without or with the kinetic effects of EPs.

4.2. Co-existence of FLEM and RWM

The co-existence of the RWM and the FLEM is computed in the tokamak configuration, as shown in figure 16, where both positive and negative rotation directions have been considered. Moreover, the kinetic effects from trapped hot ions as well as trapped thermal particles are considered in the computations. For the FLEM instability, since the frequency should be determined by the resonance condition $\omega_r \approx n\omega_{da} + n\Omega$, positive (negative) plasma rotation increases (decreases) the mode frequency. However, the rotation along both directions does not significantly influence the growth rates of the FLEM, provided that the resonance condition is satisfied.

For the RWM instability, the mode frequency is much lower than that of the FLEM. With positive rotation $\Omega > 0$, the RWM can be stabilized by the kinetic damping contributed by the precession drift of trapped thermal particles [18, 28–32], at a very slow rotation velocity ($\Omega/\omega_A \lesssim 0.014$ as shown in figure 16). No resonance-induced stabilization occurs due to the EPs. With negative rotation $\Omega < 0$, both hot and thermal ions contribute

to the drift kinetic energy δW_k^i. The RWM is stabilized with relatively slow (or even vanishing) negative rotation, mainly due to the contribution of trapped thermal particles. As rotation frequency becomes more negative, the RWM is again stabilized, but this time mainly by the kinetic damping of hot ions. Detailed investigation of these RWM phenomena will be reported elsewhere. A key observation, presented by this figure, is the co-existence of both unstable FLEM and RWM. In the parameter ranges that we investigated here, no mode coupling occurs, unlike in the RFP case. This may be related to the fact that the Doppler shift $n\Omega$ introduced by negative plasma rotation, with $n = 1$ in the tokamak case, frequency does not decrease the FLEM frequency as rapidly as in the RFP case with $n = 6$. Thus, before the FLEM frequency decreases and reaches the RWM frequency (near zero), the RWM has already been stabilized by the kinetic damping of EPs.

The eigenfunctions of the co-existing FLEM and RWM are compared in figure 17, for (*a*) the radial displacements $|\xi_1|$ associated with the most important poloidal harmonics ($n = 1$, $m = -1$ to -4), and (*b*) the radial components of the perturbed magnetic field $|Q_1|$. These two coexisting modes correspond to the case of $\Omega/\omega_A = 0.02$ from figure 16. The kinetic effects contributed from both hot ions and trapped thermal particles are considered (the curves marked with 'th + hot' in figure 16). Figure 17 presents both non-resonant poloidal harmonics ($n = 1$, $m = -1, -4$) and resonant harmonics ($n = 1$, $m = -2, -3$). Similar to the RFP case, the eigenfunctions of FLEM and RWM are of comparable shape in general. However, the perturbations of the FLEMs are pushed towards the plasma center due to the 'ideal-like' wall, and show lower amplitude of the displacements compared to that of the RWMs. The radial field perturbation $|Q_1|$ nearly vanishes at the wall for the FLEM, whilst it remains finite and extends into the outer vacuum for the RWMs.

4.3. FLEM Damping by thermal particles

Similar to the RFP plasma, passing thermal ions provide ion acoustic Landau damping on the FLEM instability also in the tokamak. Figure 18 shows various energy components. In particular, the imaginary parts of the drift kinetic energy δW_k^i contributions from EPs and from thermal particles have opposite signs and thus (partially) cancel each other.

Therefore, by including the kinetic effects of thermal particles in the tokamak computations, the FLEM instability becomes weaker compared to the case of considering only the hot ions. This leads to the requirement of higher β value for triggering the instability, and also results in lower growth rates of FLEM, as already demonstrated in figure 13.

On the other hand, the damping from thermal particles on the FLEM does not seem to substantially modify the driving force by EPs—the cancellation of the thermal particle contribution to δW_k^i is relatively small compared to that in the RFP plasma. Comparison between figures 18 (for tokamak) and 10 (for RFP) supports this conclusion. As already mentioned, the stronger cancellation in the RFP plasma is due to the shorter connection length, and thus the stronger Landau damping
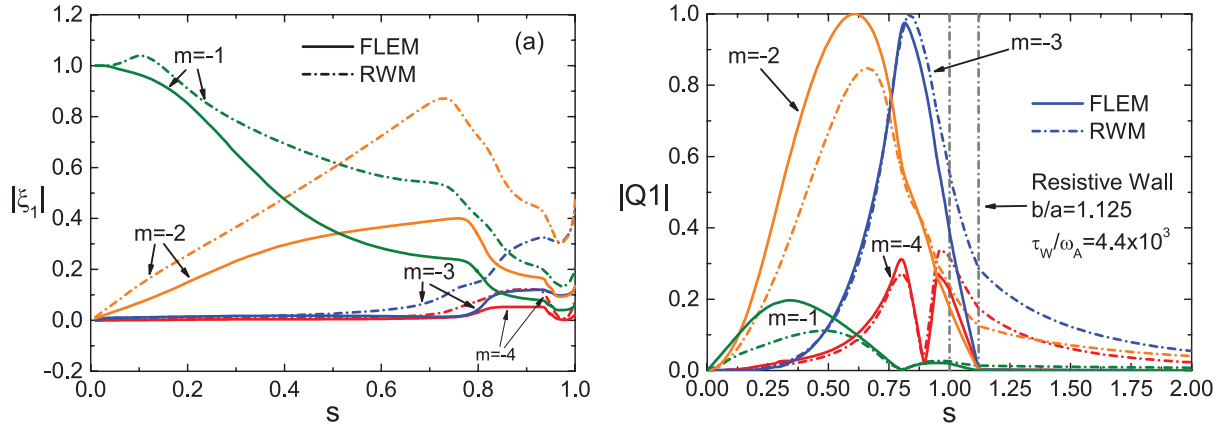
Figure 17. The radial components of (*a*) the plasma displacement $|\xi_1|$ and (*b*) the perturbed magnetic field $|Q_1|$ ($n=1$, $m=-1$ to -5), plotted along the plasma minor radius, for the FLEM and the RWM, for the point from figure 16 with full kinetic contribution and at the plasma rotation of $\Omega/\omega_A = 0.02$. The other parameters are chosen as the same as those in figure 16.
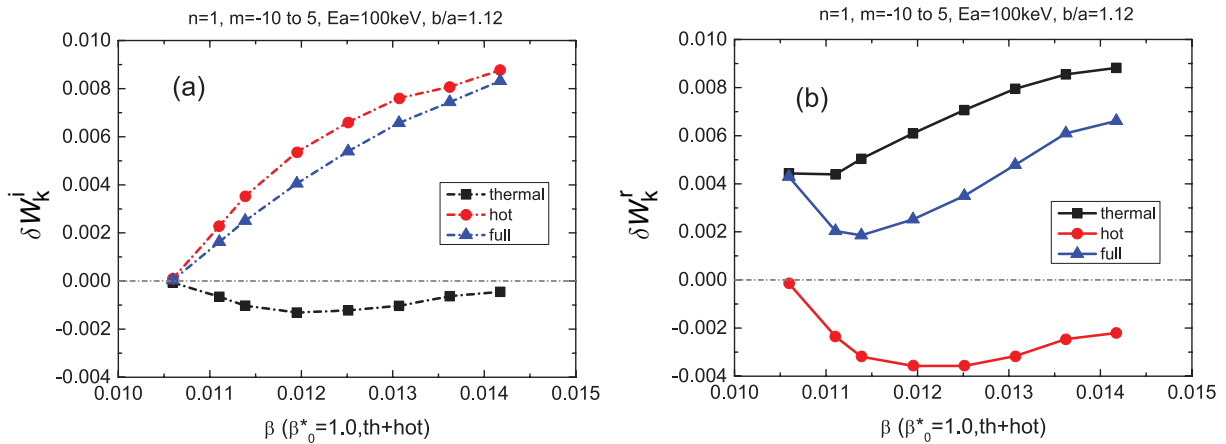

Figure 18. The drift kinetic energy components (*a*) δW_k^i, and (*b*) δW_k^r, versus the plasma beta β, computed by including kinetic resonances of both EPs and thermal particles. The corresponding stability curve is marked as 'th + hot' in figure 13. The contributions to δW_k by various species are presented as follows: the curve 'thermal' denotes the contribution from thermal particles, 'hot' denotes the contribution from energetic ions, and 'full' denotes the combination of both species. The parameters used are the same as those in figure 13 for curve 'th + hot' with $\beta_0^* = 1.0$ ($\beta^* = 0.19$).

by passing thermal particles than that in tokamaks. Similar observation has also been made in the studies of other types of instabilities [33–35] in RFP plasmas.

5. Summary and discussion

In this work, we have numerically investigated the fishbone-like external kink mode (FLEM) driven by the precessional drift motion of trapped EPs. Both RFP and Tokamak (with circular cross section) magnetic configurations are considered and the results are compared. The toroidal MHD-kinetic hybrid stability code MARS-K was used for this purpose. The code self-consistently takes into account the drift kinetic effects of both thermal and EPs. Detailed numerical analyses of the results have been performed, in order to gain better insight into the mode physics. The physics nature of the FLEM is presented, and its relation with the RWM is discussed.

The FLEM instability is numerically predicted for RFP plasmas as a non-resonant mode, which is the least stable kink mode in RFP configuration. In the presence of a sufficiently large fraction of EPs in the plasma, and with the satisfaction of the resonance condition $n\omega_{da} \approx \omega_r - n\Omega$, the stable non-resonant ideal kink mode (stabilized by a close-fitting ideal conducting wall) is converted into an unstable FLEM by the precessional drift resonance of EPs (hot ions). The mode frequency is linked to the precessional drift frequency of EPs, and therefore, is much higher than the RWM and around the ideal MHD time scale, and varies with the plasma rotation frequency. The FLEM instability occurs at rather high plasma beta β_p. In fact, the value of ideal beta limit β_p^{ideal} is the upper-bound of the parameter space for the FLEM instability. Near (and below) this boundary, the external ideal kink stays marginally stable with an ideal wall, and is thus the easiest one to be excited by EP kinetic resonances. From another point of view, the energy component δW_b is sufficiently small as the β_p value stays close but below β_p^{ideal}, resulting in a low-frequency ω_r for the external kink mode, which can then easily match the precession frequency ω_{da} of EPs. For given parameters

$(\varepsilon_\alpha, \beta^*)$ of EPs, δW_b increases as the total plasma beta β_p decreases, due to decreasing $|\delta W_F|$ (i.e. farther from the marginal state). Thus, the external kink frequency ω_r increases with decreasing β_p (equation (22A)). When ω_r becomes too large, to satisfy the resonance condition with the precession frequency ω_{da} of EPs, the instability disappears. The higher the fraction of EPs (i.e. with higher β^*), the larger the kinetic contribution to δW_k^i is expected, resulting in easier excitation of the FLEM instability. Furthermore, higher birth energy ε_α leads to higher precession frequency of EPs, which sensitively enlarges the parameter space for the FLEM triggering.

In general, the instability of FLEM does not depend on the wall resistivity. However, the wall position can significantly affect the mode's property. The closer the wall to the plasma, the higher the plasma beta required for the excitation of the instability. The kinetic effect of the thermal particles (transit resonance of passing particles) can partially cancel the driving mechanism contributed by the precession resonance of EPs, thus playing a stabilizing role on FLEMs.

In the presence of EPs, the FLEM and the RWM can coexist. They can couple to each other if plasma rotates, depending on the plasma parameters. However, the RWM can be stabilized by the plasma flow, whilst the FLEM remains unstable with the typical plasma rotation.

The same type of EP-driven instability is also computed for the tokamak plasma, where the (dominant) non-resonant external kink component (e.g. $m = 1$, $n = 1$) couples with the resonant external kink components (e.g. $m = 2, 3$; $n = 1$). The similar nature of FLEM, to that previously mentioned for RFPs, is also observed in the tokamak configuration. Therefore, in the presence of a sufficiently large fraction of trapped energetic ions in high beta plasmas, the FLEM instability may occur under the same excitation condition as discussed for RFPs. However, the computed FLEM frequency is much lower in tokamaks, than that in RFPs, due to the lower precession frequency of EPs in the former (with the same birth energy). Furthermore, the Landau damping of the transit resonance by the passing thermal particles is weaker in tokamaks than that in RFPs, due to the longer connection length in the former.

This work focuses on the physics investigation of the driven mechanism, the excitation condition, the nature of external kink instability driven by EPs, as well as the comparison of the FLEM physics between the two different configurations. The application of the current finding to the experimental observation, in a specific device, remains the next step in our future work.

Finally, we point out that, due to the non-resonant nature of the FLEM in RFP plasmas, where the $n = 6$ mode with the most important poloidal harmonics (e.g. $m = -5$ to 5) are all non-resonant, the Alfven continuum damping seems to be rather weak and does not crucially influence the nature of the instability. As for the tokamak case, although the non-resonant harmonic ($n = 1$, $m = 1$) is still the dominant component, it does couple to certain resonant components. However, we have so far not been able to identify any dramatic modification of the FLEM physics due to the coupling between the non-resonant and the resonant harmonics. This peculiar point may nevertheless deserve further investigation in the future.

References

[1] Troyon F., Gruber R., Saurenmann H., Semenzato S. and Succi S. 1984 *Plasma Phys. Control. Fusion* **26** 209
[2] Chu M.S. and Okabayashi M. 2010 *Plasma Phys. Control. Fusion* **52** 123001
[3] McGuire K. *et al* 1983 *Phys. Rev. Lett.* **50** 891
[4] Chen L., White R.B. and Rosenbluth M.N. 1984 *Phys. Rev. Lett.* **52** 1122
[5] White R.B., Chen L., Romanelli F. and Hay R. 1985 *Phys. Fluids* **28** 278
[6] Matsunaga G. *et al* 2009 *Phys. Rev. Lett.* **103** 045001
[7] Okabayashi M. *et al* 2009 *Nucl. Fusion* **49** 125003
[8] Okabayashi M. *et al* 2011 *Phys. Plasmas* **18** 056112
[9] Matsunaga G. *et al* 2013 *Nucl. Fusion* **53** 123022
[10] Hao G.Z., Wang A.K., Liu Y.Q. and Qiu X.M. 2011 *Phys. Rev. Lett.* **107** 015001
[11] Hao G.Z., Liu Y.Q., Wang A.K. and Qiu X.M. 2012 *Phys. Plasmas* **19** 032507
[12] Nabais F. *et al* 2005 *Phys. Plasmas* **12** 102509
[13] Zonca F. *et al* 2007 *Nucl. Fusion* **47** 1588–97
[14] Zonca F. *et al* 2009 *Nucl. Fusion* **49** 085009
[15] Sarff J.S. *et al* 2015 *Nucl. Fusion* **55** 104006
[16] Anderson J.K. *et al* 2013 *Phys. Plasmas* **20** 056102
[17] Lin L. *et al* 2013 *Phys. Plasmas* **20** 030701
[18] Liu Y.Q., Chu M.S., Chapman I.T. and Hender T.C. 2008 *Phys. Plasmas* **15** 112503
[19] Antonson T.M. and Lee Y.C. 1982 *Phys. Fluids* **25** 132
[20] Porcelli F., Stankiewicz R., Kerner W. and Berk H.L. 1994 *Phys. Plasmas* **1** 470
[21] Liu Y.Q., Bondeson A., Fransson C.M., Lennartson B. and Breitholtz C. 2000 *Phys. Plasmas* **7** 3681
[22] Liu Y.Q. *et al* 2014 *Phys. Plasmas* **21** 056106
[23] Bernstein I.B., Frieman E.A., Kruskal M.D. and Kulsrud R.M. 1958 *Proc. R. Soc.* A **244** 17–40
[24] Freidberg J.P. 1987 *Ideal Magnetohydrodynamics* (New York: Plenum)
[25] Hu B., Betti R. and Manickam J. 2005 *Phys. Plasmas* **12** 057301
[26] Wang Z.R., Guo S.C., Shi L., Bolzonella T., Baruzzo M. and Wang X.G. 2010 *Phys. Plasmas* **17** 052501
[27] Wang Z.R., Guo S.C., Liu Y.Q. and Chu M.S. 2012 *Nucl. Fusion* **52** 063001
[28] Menard J.E. 2014 *Phys. Rev. Lett.* **113** 255002
[29] Hu B. and Betti R. 2004 *Phys. Rev. Lett.* **93** 105002
[30] Chapman I.T. *et al* 2009 *Plasma Phys. Control. Fusion* **51** 055015
[31] Liu Y.Q. *et al* 2009 *Nucl. Fusion* **49** 035004
[32] Wang Z.R., Guo S.C. and Liu Y.Q. 2012 *Phys. Plasmas* **19** 072518
[33] Guo S.C. 2008 *Phys. Plasmas* **15** 122510
[34] Predebon I., Angioni C. and Guo S.C. 2010 *Phys. Plasmas* **17** 012304
[35] Liu S.F., Guo S.C., Kong W. and Dong J.Q. 2014 *Nucl. Fusion* **54** 043006